AIAA SciTech Forum
6-10 January 2025, Orlando, FL
AIAA SCITECH 2025 Forum

10.2514/6.2025-2586

Separation of a Laminar Boundary Layer Subjected to Pressure Gradients with Spanwise Variations

John Marshall Cooper *, Benjamin S. Savino†, Benjamin Kellum Cooper ‡, and Wen Wu§
Department of Mechanical Engineering, University of Mississippi, University, MS, 38677, USA

The characteristics of three-dimensional laminar separation bubbles (LSBs), compared with their two-dimensional counterparts, are studied using direct numerical simulation. A suction-blowing distribution is applied on the top boundary to induce flow separation. Two levels of suction-blowing strength are tested. The spanwise extent of the suction-blowing profile is varied using a Gaussian distribution centered about the domain midspan. Two non-uniform distributions (implying a three-dimensional LSB) are compared with the suction-blowing profile applied across the full span (implying a two-dimensional LSB), totaling six cases. All cases are performed at $Re = U_\infty \delta / \nu = 1000$. Results indicate stark contrast between three-dimensional and two-dimensional LSBs. In a mean sense, the widths of the three-dimensional LSBs can exhibit streamwise dependence, with a narrow 'waist' forming near their streamwise center. The instantaneous topology of the three-dimensional LSBs can be asymmetric when the three dimensionality is moderate. In such case, a dual-wake pattern consisting of long hairpin vortices dominates the reattachment and turbulent reattachment region, differing from the spanwise-oriented roller vortices commonly observed in two-dimensional LSBs.

I. Introduction

Non-uniform pressure gradients (PGs) and three-dimensional (3D) separation bubbles are ubiquitous in engineering settings. For example, wind turbine blades often feature variable chords, airfoil cross-sections, and twist angles along their span, resulting in variations of flow quantities in the spanwise direction [1]. Similarly, gas turbines experience highly three-dimensional flow due to the complex geometry of the blades, including three-dimensional separation near the leading edge of the blade and the base wall [2, 3]. Further, the tip vortices of finite-aspect-ratio wings have been shown to lead to spanwise variations of flow quantities and LSBs [4–6].

Despite the prevalence of 3D flows in engineering, studies performed to characterize the behavior and influence of separation bubbles often focus on two-dimensional (2D) configurations that are homogeneous in the spanwise/transverse direction. For experimental works, this implies that the aspect ratio of the test section is sufficient such that side-wall effects are minimal, mimicking an infinite span [7, 8]. Or, only the quasi-2D part of the flow near the mid span of test sections is used to analyze the flow. For computational studies, spanwise homogeneity is ensured by employing a spanwise uniform geometry or PGs, along with the use of periodic boundary conditions[9, 10]. While the cited studies, among a plethora of others, have provided valuable insight into the behavior of two-dimensional separating flows, 3D ones are far less investigated.

The majority of literature on 3D separating flows focus on flow over 3D geometries such as hills, bumps, and spherical protuberances [11–16]. The observed 3D behaviors are a product of the interaction of various coherent structures, including the separating flow itself, spanwise-oriented roller vortices generated by Kelvin-Helmholtz instability in the shear layer, von Kármán vortex street generated by the side surfaces of the object, etc. Thus, the results are strongly dependent on the geometry that induces the flow separation. Meanwhile, separation over a flat plate that eliminates the geometry dependence has been widely used to isolate the pressure gradient effects [17–19], yet remain limited to 2D separation flows. Jacobi et al. [20] are among the few that studies separation on a flat plate generated by 3D PGs. They reported the Reynolds number effects and observed that either a closed separation bubble or an open one can be formed by 3D PGs.

This study aims to explore the effects of various levels of three-dimensionality on the flow separation over a flat plate, avoiding the surface curvature effects as in Ref. [20]. We employed 3D freestream pressure gradients in direct numerical

*Master's student and AIAA member
†Ph.D. Candidate and AIAA member
‡Master's student and AIAA member
§Assistant Professor and AIAA member. Corresponding author. Email address: wu@olemiss.edu

simulations of a laminar separating boundary layer. The spanwise constraint on the 3D laminar separation bubble (LSB) is removed by using sufficiently wide spanwise domains. The three dimensionality of the LSB is controlled by the changing the spanwise extent of a suction-and-blowing velocity profile at the top boundary. In the following, we discuss methodology, followed by mean flow fields and turbulence statistics. Instantaneous flow fields are provided for insights into physical mechanisms responsible for observed 3D separating flow features.

II. Methodology

A. Problem Formulation

In this study, direct numerical simulations (DNS) of laminar boundary layers subjected to one- or two-dimensional freestream pressure gradients (PGs) are performed. We solve the incompressible Navier-Stokes equations normalized by inflow boundary layer thickness (δ) and freestream velocity (U_∞), which read as:

$$\frac{\partial u_i}{\partial x_i} = 0; \quad \frac{\partial u_i}{\partial t} + \frac{\partial u_i u_j}{\partial x_j} = -\frac{\partial p}{\partial x_i} + \frac{1}{Re}\frac{\partial^2 u_i}{\partial x_j^2}. \tag{1}$$

The Reynolds number $Re = U_\infty \delta/\nu = 1000$, where ν is the kinematic viscosity. The computational domain is $(L_x, L_y, L_z) = (90, 15, 48)\delta$ or $(90, 15, 72)\delta$ in the streamwise (x), wall-normal (y), and spanwise (z) directions, respectively. The reason for differing L_z is discussed momentarily. The z coordinate is defined with reference to the mid-span plane (i.e., $z \in [-L_z/2, L_z/2]$). A Blasius laminar boundary layer profile is prescribed at the inflow. No fluctuation is superposed. The freestream PGs are generated by a suction-blowing distribution of the wall-normal velocity component applied at the top boundary. The streamwise profile of this distribution, V_{top}, is defined as:

$$V_{\text{top}}(x) = -V_0 \sin\left[\frac{2\pi(x - x_0)}{L_x}\right] \exp\left[-a_s\left(\frac{2(x - x_0)}{L_x}\right)^b\right]. \tag{2}$$

Here, parameters are set as follows: $L_x = 50\delta$, $x_0 = 33\delta$, $a_s = 10$, and $b = 10$. This profile has been used in previous studies of laminar separation bubbles [21, 22]. Two magnitudes are tested: $V_0 = 0.65U_\infty$ and $0.85U_\infty$. Fig. 1(a) shows the one-dimensional suction-blowing profiles. To introduce a spanwise variation to the suction-blowing profile (and the resultant PGs), the $V_{\text{top}}(x)$ profile is weighted by a Gaussian distribution $\phi(z)$ in the spanwise direction, which reads:

$$\phi(z) = \exp\left[-\left(\frac{z}{z_0}\right)^2\right]. \tag{3}$$

The spanwise extent of the distribution is adjusted by the damping parameter z_0, which we vary between 5δ, 10δ, and ∞ among the cases. The peak velocity magnitude decreases by 90% by $1.517z_0$ (99% by $2.146z_0$) from the mid-span plane. $z_0 = \infty$ corresponds to $V_{\text{top}}(x)$ applied uniformly across the full span of the domain, which is the method utilized to generate spanwise (statistically) homogeneous LSBs. The three spanwise weighting profiles are shown in Fig. 1(b).

Multiplying the streamwise suction-blowing profile (Eq. (2)) with the spanwise weighting function (Eq. (3)), we get the two-dimensional suction-blowing profile of the wall-normal velocity as a function of x and z:

$$V_{\text{top2d}}(x, z) = \phi(z) V_{\text{top}}(x). \tag{4}$$

Contours of $V_{\text{top2d}}(x, z)$ are shown in Fig. 2 for $V_0 = 0.65U_\infty$. Throughout this paper, the terms 'non-uniform' and 'three-dimensional' are used interchangeably to describe cases where $z_0 = 5\delta$ and $z_0 = 10\delta$ (i.e., when the PGs are applied with the damping across the spanwise direction). 'Two-dimensional' is used to describe cases where $z_0 = \infty$ (PGs applied uniformly across the span). Similarly, 'suction strength' and 'peak suction velocity' are used interchangeably to reference the level of V_0/U_∞.

Based on the distribution of V_{top2d}, the streamwise (u) and spanwise (w) velocity components on the top boundary are set such that the mean spanwise vorticity $\omega_z = \partial V/\partial x - \partial U/\partial y$ and mean streamwise vorticity $\omega_x = \partial W/\partial y - \partial V/\partial z$ equal zero. Despite that ω_y is non-zero with the conditions used, its magnitude is very small with peak values of $O(10^{-4})$. The remaining boundary conditions are as follows: a convective boundary condition is used at the outflow. The no-slip condition is enforced on the bottom wall. A periodic boundary condition is employed in the spanwise direction. Large spanwise extents of the computational domain are employed in this study, especially for the $z_0 = 10\delta$

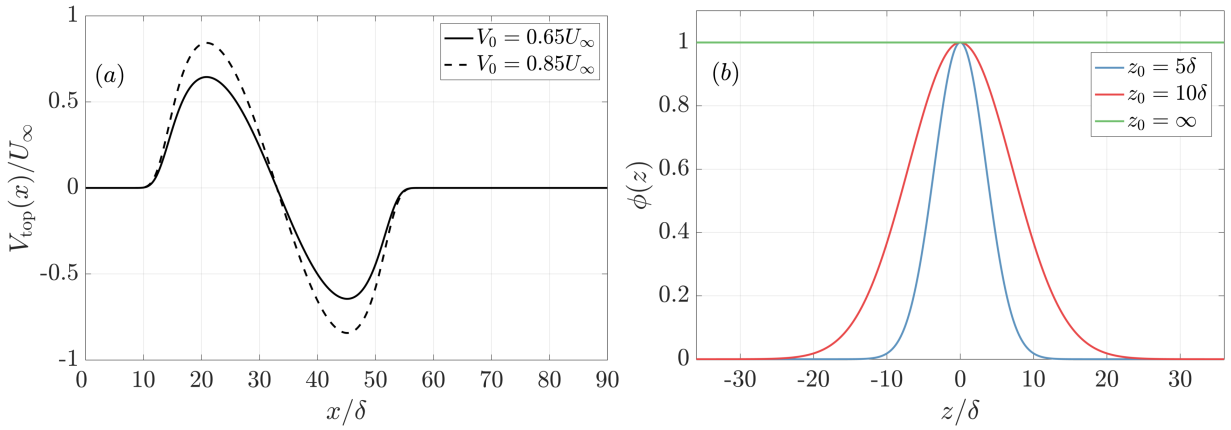

Fig. 1 (a) Streamwise profile of V_{top} for the two tested levels of V_0. (b) Weighting (damping) function utilized to introduce spanwise-variation to the top boundary condition for the three tested levels of z_0.

case. Spanwise autocorrelation of velocity fluctuations is used to ensure that the separation bubble is not confined by the spanwise domain. All correlation coefficients approach zero within $\pm 10\delta$ when $z_0 = \infty$. When $z_0 = 5\delta$ and 10δ, the turbulent fluctuations are uncorrelated within $\pm 20\delta$.

As mentioned, we test two suction strengths and three spanwise damping widths, yielding six total cases for comparison. The following nomenclature is adopted to differentiate between cases: 'zXXvYY', where 'XX' is '5', '10', or '∞' to denote $z_0/\delta = 5$, 10, and ∞. 'YY' is '65' or '85' to denote $V_0/U_\infty = 0.65$ and 0.85. Case parameters, including the domain size and grid points in each direction, are listed in Table 1.

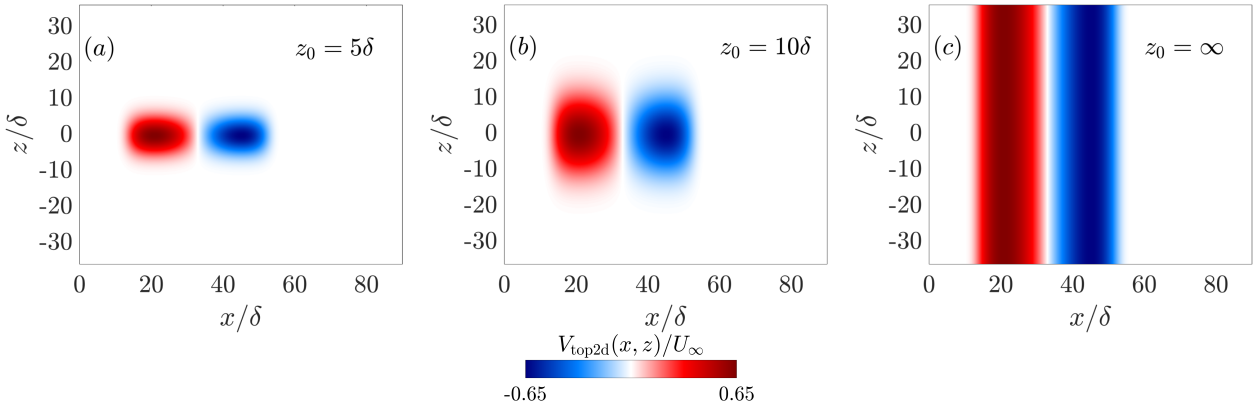

Fig. 2 Wall-normal velocity distribution applied on the top boundary ($V_{\text{top2d}}(x,z)/U_\infty$). Note only the suction level $V_0 = 0.65U_\infty$ is shown. Subplots (a), (b), and (c) display $V_{\textbf{top2d}}(x,z)$ for $z_0 = 5\delta$, 10δ, and ∞, respectively. Note that all configurations are shown on a spanwise domain of $L_z/\delta = 72$ for ease of comparison, yet the actual extent for the z5 and z∞ cases are 48δ.

B. Numerical Methods

The computational solver is a well-validated, in-house program that utilizes a second-order accurate central difference scheme for all spatial derivatives, with variables defined on a staggered grid [23–25]. Semi-implicit time advancement is employed, with a second-order Adams-Bashforth method for convective terms and an implicit Crank-Nicolson method for the viscous terms. Time is advanced with a fractional-step algorithm. The Poisson equation is solved using a pseudo-spectral method, employing a cosine transform in the streamwise direction and a fast Fourier transform in the spanwise direction, followed by a direct solve of the resulting tri-diagonal matrix [26]. The solver has demonstrated exceptional capability in our previous studies of various separating flows [27–29].

For all cases, once a statistically steady state is reached, statistics are sampled every $10\delta/U_\infty$ for a total of $10,000\delta/U_\infty$.

Table 1 Simulation Parameters

Case	Re	z_0/δ	V_0/U_∞	$(L_x, L_y, L_z)/\delta$	(N_i, N_j, N_k)	$\max(\Delta y_1^+)$
z5v65	1000	5	0.65	(90,15,48)	(1152,199,384)	0.35
z5v85	1000		0.85			0.40
z10v65	1000	10	0.65	(90,15,72)	(1152,199,576)	0.41
z10v85	1000		0.85			0.42
z∞v65	1000	∞	0.65	(90,15,48)	(1536,219,512)	0.41
z∞v85	1000		0.85			0.52

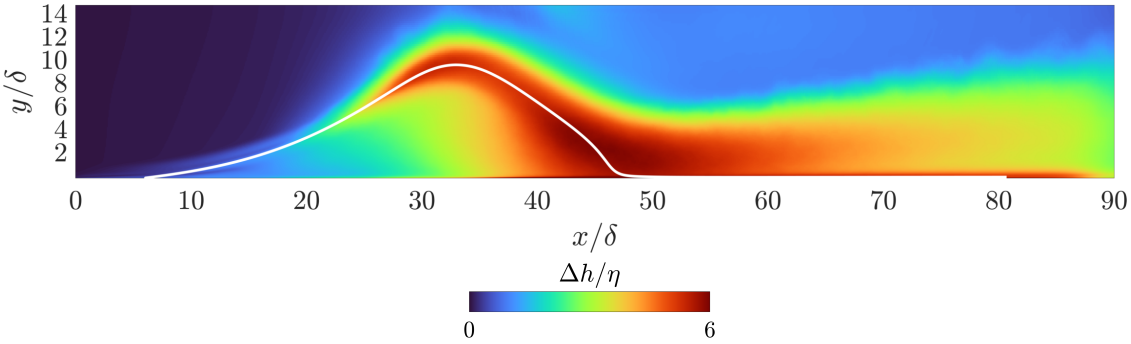

Fig. 3 Ratio of grid size to the Kolmogorov length scale ($\Delta h/\eta$) for case $z\infty v85$ grid II. The mean separating streamline is shown by the white line for reference.

This sample duration ensures that possible low-frequency motions can be captured and achieve statistically converged results. In the following discussion, capital letters (U_i) or $\overline{(.)}$ indicate 3D ensemble (time) averaged quantifies. $\langle . \rangle$ indicates quantities averaged over the region of the 3D separation bubble in the spanwise direction. Specifically, the average is taken for $z/\delta \in [-W_{\text{sep., max}}/2,\ W_{\text{sep., max}}/2]$, where $W_{\text{sep., max}}$ is the maximum width of the separation bubble (L_z for the z∞ cases). $(.)'$ indicates fluctuations from the 3D temporal average, and lowercase variables indicate instantaneous quantities.

C. Grid Refinement Study

Case z∞v85, the canonical two-dimensional separation induced by the largest APG, is used for grid refinement study. It is because such case generates the most energetic turbulent eddies and thus require the finest grid to sufficiently resolve all necessary scales of motion. Two grids are tested: the fine grid I: $N_i \times N_j \times N_k = 1536 \times 219 \times 512$; and the coarse grid II: $N_i \times N_j \times N_k = 1152 \times 199 \times 384$. Grid I is 33% × 10% × 33% more refined than grid II. Note that even the coarser one is well within the conventional resolution used for DNS: for grid II, the ratio of grid cell size ($\Delta h = \sqrt{\Delta x^2 + \Delta y^2 + \Delta z^2}$) to the Kolmogorov length scale ($\eta = (\nu^3/\epsilon)^{1/4}$, where ϵ is the turbulent kinetic energy (TKE) dissipation rate), is plotted in Fig. 3. $\Delta h/\eta \leq 6$ everywhere, much smaller than the length scale at which maximum dissipation is anticipated to occur (24η) [30]. Further, the near-wall spacing of grid II in wall units (i.e., normalized by the viscous length scale $\delta_v = \nu/u_\tau$ where u_τ is the friction velocity), denoted by superscript +, is plotted in Fig. 4. Δy_1^+, the first grid point from the wall, is maintained below 0.6. Δx^+ and Δz^+ remain below 10, indicating sufficient resolution for the wall-bounded flow. Grid I, as mentioned above, exceeds these resolutions in all three directions. Grid independence is proved by comparing the mean velocity and TKE profiles at various streamwise locations in Fig. 5. Therefore, grid II is used for the z5 and z10 three-dimensional LSB cases since it is sufficient to resolve the necessary scales of motion in the most turbulent case. For the z10 cases, N_k is increased proportionally for the larger spanwise domain.

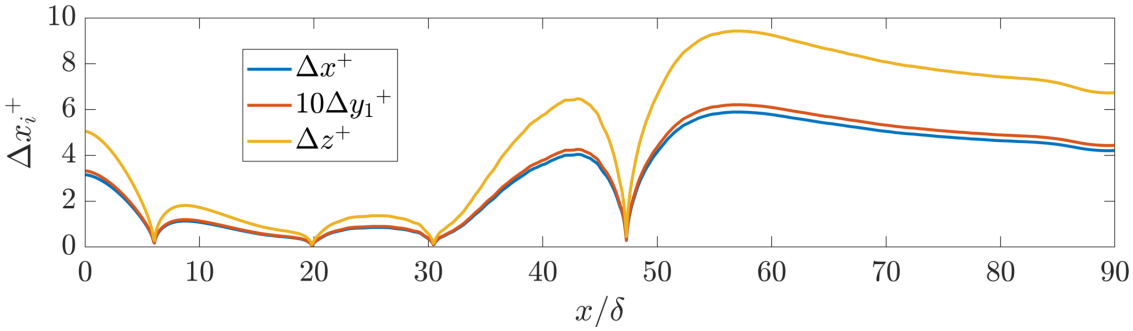

Fig. 4 Grid spacing in wall units for case z∞v85, grid II. Δy_1^+ indicates the distance to the first point from the wall and is scaled by a factor of 10 for clarity.

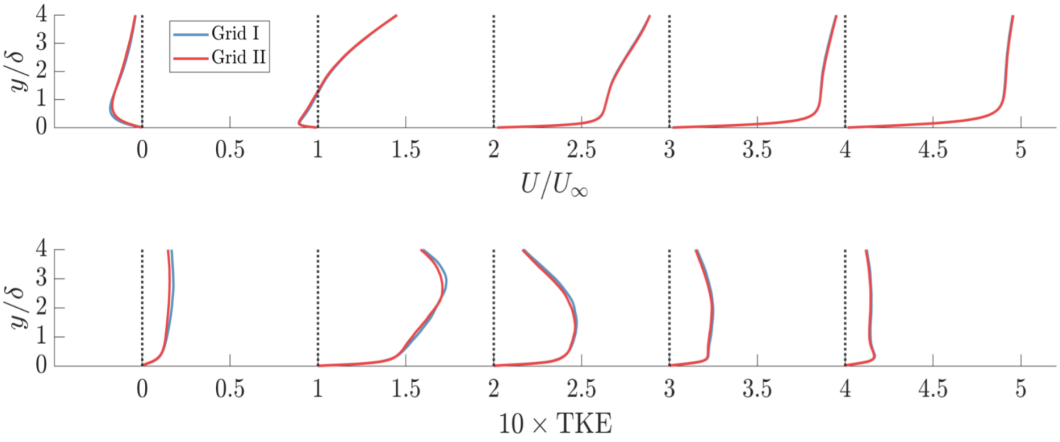

Fig. 5 Comparison of time- and spanwise-averaged streamwise velocity (top) and TKE (bottom) near the wall at select x locations. From left to right, $x/\delta = 35, 45, 55, 65, 75$. Each profile is shifted by one unit for clarity.

III. Results

A. Mean Flow

Three-dimensional isosurfaces of $U = 0$ are shown in Fig. 6, providing visualization of the time-averaged region where the flow detaches from the wall. Since the $V_{\text{top}}(x)$ and $\phi(z)$ together determine the mass extracted by the suction, stark differences shows between the two- and three-dimensional LSBs. As suction width increases for a given suction strength, the spanwise width, streamwise length, and wall-normal height of the LSB increase. The same behaviors are true for a given suction width and increasing suction strength, except for the two-dimensional cases, where case z∞v85 reattaches prior to z∞v65. Interestingly, for the three-dimensional cases, the spanwise width of the LSB varies in the streamwise direction. The upstream portion of the separation bubble is relatively wide. Then, it narrows near the center of the separation bubble especially in the vicinity of the wall. Further downstream, the separation bubble expands in the spanwise direction, exceeding its width at the beginning of the separation bubble. Such behavior is most prominent in the z10 cases, while case z5v65 shows an oval separation region without the narrow 'waist'. The streamwise length of the LSB ($L_{\text{sep.}}$), along with the minimum and maximum spanwise width ($W_{\text{sep., min.}}$ and $W_{\text{sep., max.}}$, respectively) are provided in Table 2. The topology of these 3D separation regions is qualitatively similar to one configuration studied by [20] (refer to their Fig. 8d). However, as we will show below by the instantaneous flow visualization, the turbulent structures in the wake are remarkably different.

Despite that the LSBs are not statistically homogeneous in the spanwise direction in the z5 and z10 cases, taking the spanwise averages over the 3D separation regions provides quantitative estimates for separation onset and reattachment, bulk reverse flow, and allows for comparison with conventional two-dimensional LSBs. Thus, Fig. 7 shows the spanwise regionally-averaged mean streamwise velocity. The velocity is averaged over $z/\delta \in [-W_{\text{sep., max.}}/2,\ W_{\text{sep., max.}}/2]$ to

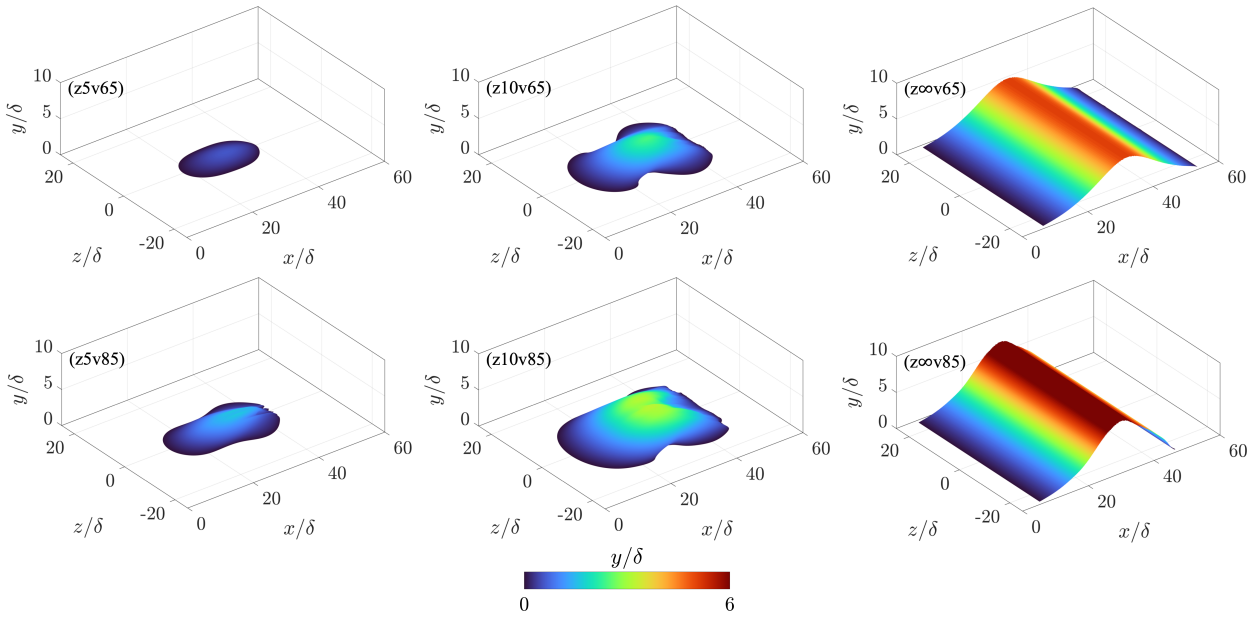

Fig. 6 Isosusrfaces of $U = 0$ colored by height from the bottom wall. The field of view is limited to $x/\delta = [0,\ 60]$, $y/\delta = [0,\ 10]$, $z/\delta = [-25,\ 25]$ for clarity. Top row: $V_0 = 0.65U_\infty$; bottom row: $V_0 = 0.85U_\infty$. Suction width increases from left to right.

Table 2 Mean Separation Bubble Metrics

Case	Re	z_0/δ	V_0/U_∞	$L_{\text{sep.}}/\delta$	$W_{\text{sep., min.}}/\delta$	$W_{\text{sep., max.}}/\delta$
z5v65	1000	5	0.65	18.9	13.4	13.4
z5v85	1000		0.85	26.2	14.5	18.8
z10v65	1000	10	0.65	29.4	13.0	28.1
z10v85	1000		0.85	36.9	19.4	30.6
z∞v65	1000	∞	0.65	47.1	48.0	48.0
z∞v85	1000		0.85	42.0	48.0	48.0

ensure that the comparison of the reverse flow is not biased by considering different amounts of forward flow outside the separation region in the spanwise direction. Streamlines calculated using the obtained 2D velocity and passing $x = 0$, $y/\delta = 0.3$, 0.5, 0.7, and 0.9 are plotted to aid in visualizing the separating shear layer. The 2D separation bubbles obtained clearly show a strong dependence on both suction strength and width. As the suction strength increases, the height of the separation bubble and the magnitude of reverse flow near reattachment increases. The same behaviors occur for increasing suction width for a fixed peak suction velocity. Increasing suction width and strength also results in steeper streamlines on the lee sides of the LSB. The discussed changes to the mean bubble are more drastic as suction width changes as opposed to changing suction strength.

The mean skin-friction coefficient ($C_f = 2\tau_w/U_\infty^2,\ \tau_w = \nu\partial\langle U\rangle/\partial y$), obtained using the spanwise-averaged mean velocity previously discussed, is plotted in Fig. 8. Color corresponds to suction width while line style corresponds to suction strength. The behavior at the separation point (defined as the x location where $C_f = 0$ and $\partial C_f/\partial x < 0$) is evident: stronger suction velocity results in earlier separation. Similarly, increased suction width also results in earlier separation. The modulation due to increasing suction width is more pronounced than that due to increased APG. The behavior of skin-friction near the reattachment point (defined as $C_f = 0$ and $\partial C_f/\partial x > 0$) is far more complex than near the separation point. For the 3D cases, the stronger suction reattaches later than the weaker one. Conversely, the two-dimensional LSB reattaches earlier when the stronger suction is applied. The length of the LSB is also listed in Table 2. Valuable insights can also be drawn from the behavior of skin friction upstream and downstream of the reattachment points in Fig. 8. As expected, the magnitude of reverse flow prior to the reattachment point increases

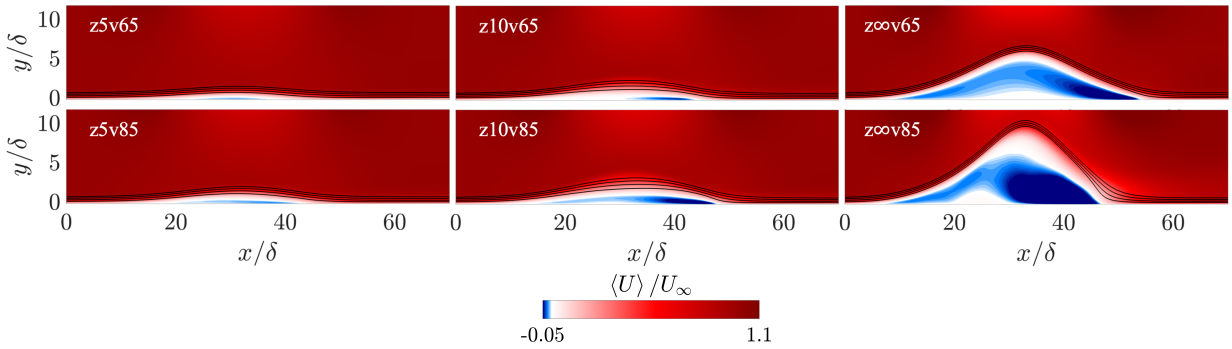

Fig. 7 Spanwise regionally-averaged streamwise velocity ($\langle U \rangle / U_\infty$). The spanwise-average is performed only over the largest width of the separation bubble $W_{\text{sep., max.}}$ (see Table 2 and text). Separating streamlines calculated with the resultant 2D velocity are plotted from $x/\delta = 0$, $y/\delta = 0.3$, 0.5, 0.7, and 0.9. The y axis is stretched by a factor of 2 for clarity.

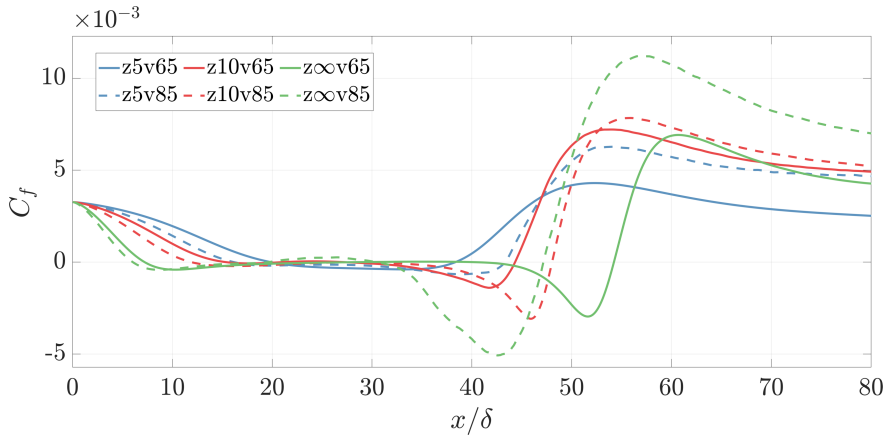

Fig. 8 Skin-friction coefficient: $C_f = 2\tau_w / U_\infty^2$ where $\tau_w = \nu \partial \langle U \rangle / \partial y$. $\langle U \rangle$ is the spanwise regionally-averaged mean streamwise velocity shown in Fig. 7. Here, suction width is denoted by color while suction strength is denoted by line style.

as APG increases (i.e., comparing the same color lines). Similarly, the magnitude of forward flow downstream of reattachment increases as APG increases. The same trends are broadly true for increasing suction width for a given APG (comparing same line-styles). It is noteworthy that the three-dimensional cases z5v85, z10v65, and z10v85 display similar (if not greater) magnitude C_f peaks downstream of reattachment to case z∞v65, despite markedly smaller separation bubbles in the former. Thus, the breakdown and reattachment mechanism of the three-dimensional LSB is likely different than that of the canonical two-dimensional LSB, and is hypothesized to generate greater turbulence and thus skin friction (relative to the LSB size) compared with the latter.

B. Turbulent Statistics

To investigate the turbulent breakdown of the separating shear layer, we plot the spanwise regionally-averaged turbulent kinetic energy, defined as TKE = $\left\langle \overline{u'u'} + \overline{v'v'} + \overline{w'w'} \right\rangle / 2$, in Fig. 9. The same streamlines as in Fig. 7 are shown by white dashed lines here. The TKE in case z∞v85 is scaled by a factor of 0.15 for clarity, as it produces significantly greater TKE than the other cases. Notably, case z5v65 displays nearly zero TKE, indicating a steady, quiescent LSB. The small separation region and weak reverse flow cannot produce sufficient shear to generate roller vortices or any other turbulent reattachment mechanisms. Despite a comparable separation bubble, and only marginal mean reverse flow (see Fig. 7), case z5v85 shows significantly higher TKE at reattachment and in the wake than case z5v65. The behavior of TKE magnitude in the LSB wake is non-monotonic when $z = 10\delta$. Significant levels of TKE form earlier in the LSB, and are larger in magnitude, in case z10v65 versus z10v85. Finally, when $z_0 = \infty$, TKE

increases with the suction strength. TKE in case z∞v85 occurs earlier in the separation bubble (prior to the LSB crest) and displays significancy greater magnitude than z∞v65.

Comparing the trends of TKE for a fixed suction strength as suction width changes (i.e., each row of Fig. 9), the behaviors are again non-monotonic. When $V_0 = 0.65U_\infty$, the largest TKE occurs for case z10v65. This implies that case z∞v65 experiences a relatively smooth reattachment versus case z10v65. The cause for augmented TKE in the latter case warrants further investigation. When $V_0 = 0.85U_\infty$, however, TKE at reattachment increases monotonically with the suction width. All these non-monotonic trends in the 2D TKE at reattachment indicates that the LSB development and breakdown mechanisms likely differ in three-dimensional cases versus two-dimensional ones. We now turn to instantaneous flow visualization to investigate the said differences.

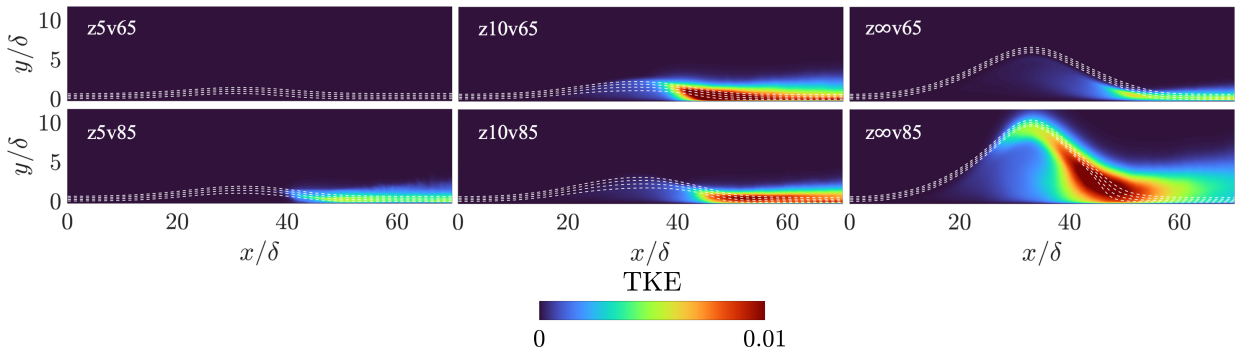

Fig. 9 Spanwise regionally-averaged turbulence kinetic energy (TKE). For case $z\infty v85$, 0.15× TKE is plotted for clarity, as this case displays significantly higher TKE than the others. Streamlines beginning at $x/\delta = 0$, $y/\delta = 0.1,\ 0.3,\ 0.5,\ 0.7$, and 0.9 are shown by the white dashed lines. The y axis is stretched by a factor of 2 for clarity.

C. Instantaneous flow field

Among other instantaneous features of the flow, strong unsteadiness at low frequencies marks the dominant spatial and temporal fluctuations of the flow. The total TKE over the entire domain exhibits periodicity with respect to such unsteadiness. Cases z5v85 and z10v85 are the two that show these phenomena most prominently, and thus we will discuss them in this section. Figure 10 exhibits the instantaneous streamwise velocity (u/U_∞) in the $x-z$ plane at the first grid point from the wall for case z5v85. Two time instances corresponding to the minimum (left) and maximum (right) total TKE in a typical unsteady cycle are chosen to compare. In both time instances, a narrow turbulent wake is formed that is 50% the maximum width of the LSB. The instantaneous wake is roughly symmetric about $z = 0$. At the time instance corresponding to minimum TKE (left plot in Fig. 10), a coherent vortex that is 'attached' to the LSB is visible, and appears to be in the process of shedding. At the time instance corresponding to maximum TKE (right plot in Fig. 10), this structure has shed from the LSB and is broken down into smaller-scale turbulence. The Strouhal number for this unsteadiness, defined as $St = fL_{\text{sep}}/U_\infty$ is about 0.11. These features are similar to the structures in the 3D separation regions observed by Jacobi et al. [20].

A different periodic behavior of the wake of the separation region was observed for case z10v85. Contours of u/U_∞ for this case is plotted in Fig. 11. Again, the $x-z$ plane is extracted at the first point from the wall. Three time instances are chosen to show the unsteadiness caused by the switching of wakes. At any time instant, a 'dual-wake' is formed in the rear end of the separating shear layer in this case, which consists of two distinct turbulent wake regions that bound a fairly quiescent region in the middle downstream of the spanwise-center of the LSB. The strongest reverse flow in the LSB occurs immediately upstream of this quiescent wake region. During an unsteady cycle, one of the wakes dominates the other, and the switching between the two leads to a low-frequency motion at Strouhal number around 0.06. In Fig. 11, the left plot represents a characteristic time instant that the turbulent wake at positive z is dominant, the middle plot is the subsequent time instant of that the two wakes are comparable, and the right plot is the subsequent instant that the negative-z wake is dominant. The total TKE is low when one of the wakes is dominant (left and right plots in Fig. 11), and peaks during the switch when both are relatively strong (middle plot).

The switching of the wake in 3D separation has been reported in previous studies of flow over 3D bumps. As mentioned in the Introduction, the switching has been contributed to the von Kármán vortex street shedding of (quasi)

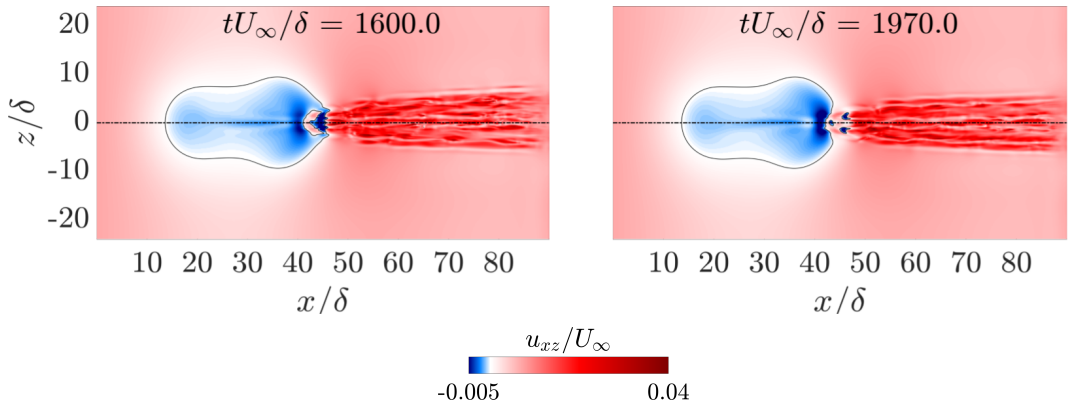

Fig. 10 Contours of instantaneous streamwise velocity (u/U_∞) for case z5v85, shown at the $x-z$ plane at the first grid point away from the wall. The horizontal dot-dash lines indicate the mid span. Solid black lines indicate the contour of instantaneous $u = 0$. See text for the details of the selected time instances.

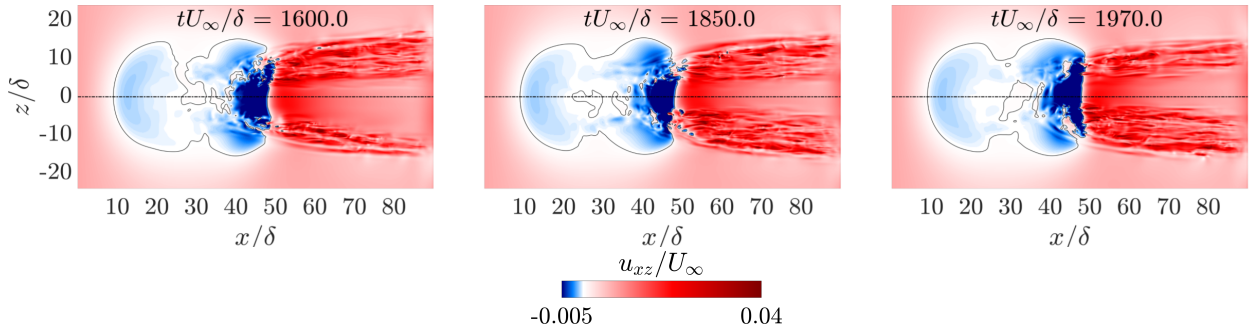

Fig. 11 Contours of instantaneous streamwise velocity (u/U_∞) for case z10v85, shown at the $x-z$ plane at the first grid point away from the wall. The horizontal dot-dash lines indicate the mid span. Solid black lines indicate the contour of instantaneous $u = 0$. See text for the details of the selected time instances.

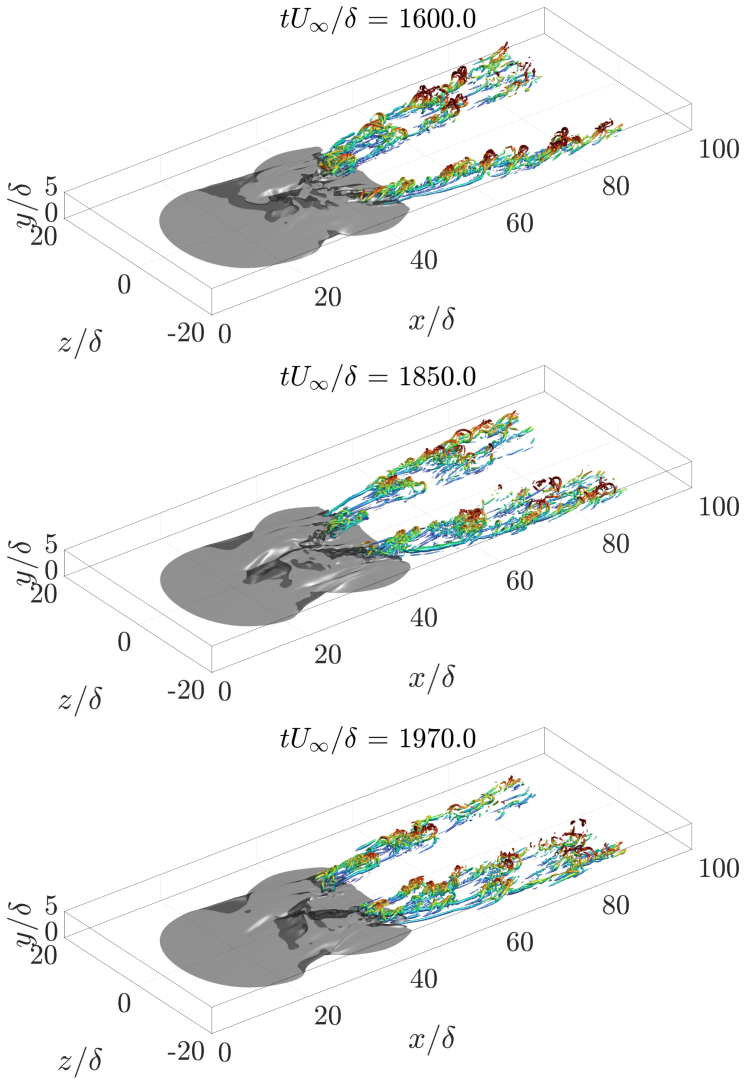

Fig. 12 Instantaneous three-dimensional flow field for case z10v85. The gray isosurfaces are of instantaneous streamwise velocity $u = 0$. The colored isosurfaces are of the second invariant of the velocity-gradient tensor $Q = 0.15U_\infty^2/\delta^2$ colored by the distance from the wall. The same three time instances displayed in Fig. 11.

wall-normal vorticity along the spanwise surfaces of the obstacle. However, we do not observe such mechanism in the current configuration. The turbulent structures in the wake at the same time instances as displayed in Fig. 11 are shown in Fig. 12, by the isosurfaces of instantaneous $u = 0$ and second invariant of the velocity gradient tensor ($Q := -(1/2)(\partial u_j/\partial x_i)(\partial u_i/\partial x_j)$). The expected spanwise-oriented roller vortices that are common in two-dimensional separating shear layers are not readily observed here regardless of the level of Q used. Instead, long streamwise-oriented structures bound the two distinct wake regions, which are characterized themselves by arched hairpin vortices. The switch in dominant wake side is clearly observed by a greater population of turbulent hairpins for $z > 0$ in the top panel, and a greater population for $z < 0$ in the bottom panel. In the middle panel of the figure, the wake structure is roughly symmetric in the middle column, with both sides exhibiting a large population of turbulent vortices.

The differences in the wake structure between case z5v85 and z10v85 highlight why the spanwise-averaged TKE (Fig. 9) is greater in case z5v85 than z10v85. In the latter, there is a quiescent wake region ($-5 \lesssim z/\delta \lesssim 5$) that was included in the spanwise regional-average we employed. This region has very low TKE, as indicated by the lack of turbulent structures in Fig. 12. Thus, the spanwise-average included a region of low TKE, reducing the kinetic energy per unit span. Case z5v85, however, has a fully turbulent wake. Thus, on a per-unit-span basis, the TKE is greater. This highlights the necessity to investigate and characterize the 3D LSBs from a three-dimensional viewpoint, as the

dynamics and statistics can clearly vary in the spanwise direction.

IV. Conclusion

Direct numerical simulations (DNS) are employed to investigate the effects of freestream pressure gradients (PGs) with spanwise variations on laminar separation bubble (LSBs). Our results indicate various qualitative differences between canonical, two-dimensional LSBs and three-dimensional LSBs generated by spanwise inhomogeneous PGs. The suction width is shown to have a more significant impact on both the mean separation point than the suction strength in the current configuration. Fundamental qualitative differences are observed in the topology and vortex structure of three-dimensional LSBs in comparison with their two-dimensional counterparts. Periodicity in the three-dimensional LSB and wake structure was identified. A very narrow region of freestream PG leads to a single-wake separation bubble, which undergoes periodic shedding of vortices that alters a high fluctuation wake in the mid span. When the three-dimensionality of the PGs is moderate, the LSB displays asymmetry, forming two wakes consisting of hairpin vortices. The two wakes bound a quiescent, laminar reattachment region downstream of the mid span of the LSB. The side that was dominant switched periodically. Rather than the canonical spanwise-oriented roller structures dominating the separating shear layer and reattachment, streamwise-oriented vortices are found to form in the lee-side of the LSB and extend through the turbulent wake for this case. Ongoing work includes quantification of the spatio-temporal dynamics of the LSBs, identification of the mechanisms that cause the wake switching, as well as control of the 3D separation bubble.

Acknowledgments

The authors gratefully acknowledge the San Diego Supercomputer Center (SDSC) Expanse CPU cluster for computing resources. W.W. acknowledges the support from NSF grant OIA-2131942, monitored by Dr. Hongmei Luo. B.S. acknowledges support from NSF GRFP Award 2235036.

References

[1] Schubel, P. J., and Crossley, R. J., "Wind Turbine Blade Design," *Energies*, Vol. 5, 2012, pp. 3425–3449.

[2] Langston, L. S., Nice, M. L., and Hooper, R. M., "Three-Dimensional Flow Within a Turbine Cascade Passage," *J. Eng. P.*, 1977, pp. 21–28.

[3] Hah, C., "A Navier-Stokes Analysis of Three-Dimensional Turbulent Flows Inside Turbine Blade Rows at Design and Off-Design Conditions," *J. Eng. Gas. Turb. Power*, Vol. 106, 1984, pp. 421–429.

[4] Taira, K., and Colonius, T., "Three-dimensional flows around low-aspect-ratio flat-plate wings at low Reynolds numbers," *J. Fluid Mech.*, Vol. 623, 2009, pp. 187–207.

[5] DeVoria, A. C., and Mohseni, K., "On the mechanism of high-incidence lift generation for steadily translating low-aspect-ratio wings," *J. Fluid Mech.*, Vol. 813, 2017, pp. 110–126.

[6] Zhu, Y., Wang, J., Xu, Y., Qu, Y., and Long, Y., "Swallow-tailed separation bubble on a low-aspect-ratio trapezoidal plate: effects of near-wall spanwise flow," *J. Fluid Mech.*, Vol. 965 A12, 2023, pp. 1–18.

[7] Horton, H. P., "Laminar separation bubbles in two and three dimensional incompressible flow," Ph.D. thesis, Queen Mary University of London, 1968.

[8] O'Meara, M. M., and Mueller, T. J., "Laminar Separation Bubble Characteristics on an Airfoil at Low Reynolds Numbers," *AIAA Journal*, Vol. 25, No. 8, 1987, pp. 1033–1041.

[9] Pauley, L. L., Moin, P., and Reynolds, W. C., "The structure of two-dimensional separation," *J. Fluid Mech.*, Vol. 220, 1990, pp. 397–411.

[10] Alam, M., and Sandham, N. D., "Direct numerical simulation of 'short' laminar separation bubbles with turbulent reattachment," *J. Fluid Mech.*, Vol. 410, 2000, pp. 1–28.

[11] Garcia-Villalba, Li, N., Rodi, W., and Leschziner, M. A., "Large-eddy simulation of separated flow over a three-dimensional axisymmetric hill," *J. Fluid Mech.*, Vol. 627, 2009, pp. 55–96.

[12] Byun, G., and Simpson, R. L., "Surface-Pressure Fluctuations from Separated Flow over an Axisymmetric Bump," *AIAA J.*, Vol. 48, 2010, pp. 2397–2405.

[13] Woszidlo, R., Taubert, L., and Wygnanski, I., "Manipulating the Flow over Spherical Protuberances in a Turbulent Boundary Layer," *AIAA J.*, Vol. 47, 2009, pp. 437–450.

[14] Patel, N., and Menon, S., "Structure of flow separation and reattachment behind an axisymmetric hill," *J. Turbul.*, Vol. 8, 2007, pp. 1–24.

[15] Ching, D. S., Elkins, C. J., and Eaton, J. K., "Investigation of geometric sensitivity of a non-axisymmetric bump: 3D mean velocity measurements," *Exp. Fluids*, Vol. 59, 2018, p. 143.

[16] Tu, H., Wang, Z., Gao, Q., She, W., Wang, F., Wang, J., and Wei, R., "Tomographic PIV investigation on near-wake structures of a hemisphere immersed in a laminar boundary layer," *J. Fluid Mech.*, Vol. 971, 2023, p. A36.

[17] Na, Y., and Moin, P., "Direct numerical simulation of a separated turbulent boundary layer," *J. Fluid Mech.*, Vol. 374, 1998, p. 379–405.

[18] Wu, W., and Piomelli, U., "Effects of surface roughness on a separating turbulent boundary layer," *J. Fluid Mech.*, Vol. 841, 2018, pp. 552–580.

[19] Abe, H., "Direct numerical simulation of a turbulent boundary layer with separation and reattachment over a range of Reynolds numbers," *Fluid Dyn. Res.*, Vol. 51, 2019, p. 011409.

[20] Jacobi, R., Wernz, S., and Fasel, H. F., "Numerical Investigation of Localized Separation Induced by a Three-Dimensional Pressure Gradient," *38th Fluid Dynamics Conference and Exhibit (AIAA 2008-4056)*, 2008.

[21] Seo, J. H., Cadieux, F., Mittal, R., Deem, E., and Cattafesta, L., "Effect of synthetic jet modulation schemes on the reduction of a laminar separation bubble," *Phys. Rev. Fluids*, Vol. 3, 2018, p. 033901.

[22] Wu, W., Seo, J. H., Meneveau, C., and Mittal, R., "Response of a Laminar Separation Bubble to Forcing with Zero-Net Mass Flux Jets," *2018 Flow Control Conference, AIAA AVIATION Forum, (AIAA 2018-4018)*, 2018.

[23] Keating, A., Piomelli, U., Bremhorst, K., and Nešić, S., "Large-eddy simulation of heat transfer downstream of a backward-facing step," *J. Turbul.*, Vol. 5, No. 20, 2004, pp. 1–27.

[24] Wu, W., Piomelli, U., and Yuan, J., "Turbulence statistics in rotating channel flows with rough walls," *Intl. J. Heat Fluid Flow*, Vol. 80, 2019, p. 108467.

[25] Wu, W., and Savino, B. S., "Dynamics of pore flow between shark dermal denticles," *CTR Annual Research Briefs*, 2023, pp. 197–208.

[26] Moin, P., *Fundamentals of Engineering Numerical Analysis*, Cambridge University Press, 2010.

[27] Wu, W., and Piomelli, U., "Effects of surface roughness on a separating turbulent boundary layer," *J. Fluid Mech.*, Vol. 841, 2024, pp. 552–580.

[28] Savino, B. S., and Wu, W., "Impact of spanwise rotation on flow separation and recovery behind a bulge in channel flows," *J. Fluid Mech.*, Vol. 999, 2024, p. A51. https://doi.org/doi:10.1017/jfm.2024.898.

[29] Savino, B. S., and Wu, W., "Thrust generation by shark denticles," *J. Fluid Mech.*, Vol. 1000, 2024, p. A80. https://doi.org/doi:10.1017/jfm.2024.978.

[30] Pope, S. B., *Turbulent Flows*, Cambridge University Press, 2000.